

REPORT DOCUMENTATION PAGE

Public reporting burden for this collection of information is estimated to average 1 hour per response, including the time for reviewing gathering, and maintaining the data needed, and completing and reviewing the collection of information. Send comments regarding this burden estimate or any other aspect of this collection of information, including suggestions for reducing this burden to Washington Headquarters Service, Directorate for Information Operations and Reports, 1215 Jefferson Davis Highway, Suite 1204, Arlington, VA 22202-4302, and to the Office of Management and Budget, Paperwork Reduction Project (0704-0188) Washington, DC 20503.

AFRL-SR-AR-TR-08-0145

PLEASE DO NOT RETURN YOUR FORM TO THE ABOVE ADDRESS.

1. REPORT DATE (DD-MM-YYYY)		2. REPORT TYPE Final Technical Report		3. DATES COVERED (From - To) 1 June 2006 - 30 November 2007	
4. TITLE AND SUBTITLE Understanding Micro-Ramp Control for Shock Boundary Layer Interactions				5a. CONTRACT NUMBER	
				5b. GRANT NUMBER FA9550-06-1-0400	
				5c. PROGRAM ELEMENT NUMBER	
6. AUTHOR(S) Dr. Eric Loth				5d. PROJECT NUMBER	
				5e. TASK NUMBER	
				5f. WORK UNIT NUMBER	
7. PERFORMING ORGANIZATION NAME(S) AND ADDRESS(ES) University of Illinois Aerospace Engineering Urbana IL 61801				8. PERFORMING ORGANIZATION REPORT NUMBER	
9. SPONSORING/MONITORING AGENCY NAME(S) AND ADDRESS(ES) USAF/AFRL AFOSR 875 North Randolph Street Arlington VA 22203				10. SPONSOR/MONITOR'S ACRONYM(S) AFOSR	
				11. SPONSORING/MONITORING AGENCY REPORT NUMBER N/A	
12. DISTRIBUTION AVAILABILITY STATEMENT Distribution Statement A: Approved for public release. Distribution is unlimited.					
13. SUPPLEMENTARY NOTES					
14. ABSTRACT Micro-vortex generators (μ VGs) have the ability to alter the near-wall structure of compressible turbulent boundary layers in such a way that the flow becomes significantly less susceptible to separations and more stable to unsteady disturbances. Due to their extremely small size, μ VGs are embedded in the boundary layer and may provide reduced viscous drag when compared to traditional vortex generators. Of several candidate μ VGs, micro-ramps have been found to significantly impact shock boundary layer interaction flows, while being cost-effective, physically robust, and requiring no power sources. Thus detailed study of flow interactions with micro-ramps on a supersonic boundary layer at $M=3.0$ was investigated using monotone integrated Large Eddy Simulations (MILES) and Reynolds Averaged Navier-Stokes (RANS). A rescaling method was used to efficiently generate turbulent inflow conditions. Studies showed that the vortical structure generated from the micro-ramp flows through the separation region caused by the impinging shock, which helped to reduce the area of separation.					
15. SUBJECT TERMS					
16. SECURITY CLASSIFICATION OF:			17. LIMITATION OF ABSTRACT	18. NUMBER OF PAGES 28	19a. NAME OF RESPONSIBLE PERSON
a. REPORT Unclassified	b. ABSTRACT Unclassified	c. THIS PAGE Unclassified	Unclassified		19b. TELEPHONE NUMBER (Include area code) (703)

Final Report for:

AFSOR GRANT

AF FA9550-06-1-0400 AF FA9550-06-1-0400

**Understanding Micro-Ramp control for Shock Boundary
Layer Interactions**

Grant Period 6/1/06-11/30/07

Report: 2/7/2008

**Eric Loth and Sang Lee
University of Illinois
Urbana-Champaign**

20080331074

Table of Contents

Nomenclature	3
Abstract	4
I. Introduction	4
II. Numerical Methodology	5
2.1 Numerical Schemes and Turbulence Models	
2.2 Rescaling-Recycling Method	
2.3 Computational Domain	
2.4 Spatial Independence and Time Integration Study	
III. Results	9
3.1 Supersonic boundary layer flow with micro-ramp and no shock wave	
3.2 SBLI with no micro-ramp	
3.3 SBLI with micro-ramp	
3.4 Micro-ramp size and location	
IV. Conclusions	12
V. References	13
VI. Figures	14

Nomenclature

β	= frictional velocity ratio
cfl	= Courant number
δ	= boundary layer thickness
δ_{ref}^*	= displacement thickness at x_{IS} but with no shock effects
h	= micro-ramp height
η	= wall normal coordinate normalized by boundary layer thickness
κ	= von Karman constant
M	= Mach number
Re_{ref}	= Reynolds number based on δ_{ref}^*
Δt	= time step
T	= temperature
τ	= integration time scale
U	= average streamwise velocity
u	= instantaneous streamwise velocity
u'	= streamwise fluctuation velocity
u_τ	= frictional velocity
ν_ω	= kinematic viscosity at wall
v	= wall normal velocity
w	= spanwise velocity
W	= weighting function
x^*	= streamwise distance referenced by $(x - x_{IS})/\delta_{ref}^*$
x_{IS}	= shock impingement point
y^*	= transverse distance referenced by $(y - y_{wall})/\delta_{ref}^*$
y_{wall}	= floor of the domain
z^*	= spanwise distance referenced by $(z - z_{rc})/\delta_{ref}^*$
z_{rc}	= micro-ramp center

Abstract

Micro-vortex generators (μ VGs) have the ability to alter the near-wall structure of compressible turbulent boundary layers in such a way that the flow becomes significantly less susceptible to separations and more stable to unsteady disturbances. Due to their extremely small size, μ VGs are embedded in the boundary layer and may provide reduced viscous drag when compared to traditional vortex generators. Of several candidate μ VGs, micro-ramps have been found to significantly impact shock boundary layer interaction flows, while being cost-effective, physically robust, and requiring no power sources. Thus detailed study of flow interactions with micro-ramps on a supersonic boundary layer at $M=3.0$ was investigated using monotone integrated Large Eddy Simulations (MILES) and Reynolds Averaged Navier-Stokes (RANS). A rescale-recycle method was used to efficiently generate turbulent inflow conditions. Studies showed that the vortical structure generated from the micro-ramp flows through the separation region caused by the impinging shock, which helped to reduce the area of separation. Three cases of micro-ramp configurations were studied; 1) base line micro-ramp, 2) micro-ramp reduced to half size and 3) the same smaller device placed closer to the shock impingement. Among the three configurations, the second case gave better performance in terms of the displacement thickness and total pressure recovery, though none completely eliminated the flow separation region. In general, the LES predictions were superior to the RANS results but were much more computationally intensive.

I. Introduction

The performance of supersonic engine inlets is critically affected by shock wave / boundary layer interactions (SBLIs) occurring throughout the supersonic portion of the flow. Most of these interactions are caused by oblique shock waves, but the final interaction is usually due to a normal shock. In all these cases the boundary layers growing along the walls of the intake are subjected to severe adverse pressure gradients which can cause boundary layer separation, unsteady flow, and even engine un-start. Currently such problems are avoided primarily through the use of boundary layer bleed/suction. This control method is able to suppress shock induced separation and it can also fix the location of the final shock wave which helps to prevent shock oscillations and flow unsteadiness. However, bleed mass flow rates have to be considerable to achieve the desired control effect (as much as 10-20% of intake mass flow at high Mach numbers) and this is a source of significant performance degradation. The intention of this study is to investigate a novel type of flow control device that may be able to offer similar control benefits and deliver a considerable reduction of the required bleed mass flow rate. As long as these gains are achievable with negligible drag increase while retaining stability, the overall advantage of such flow control could be highly significant.

Among the multitude of novel flow control methods suggested in recent years, sub-boundary layer vortex generators (SBVGs) are particularly interesting because they combine the well-demonstrated capability of vortex generators (VGs) to suppress or delay separation with a significantly reduced device drag. In recent computations performed by NASA Glenn Research Center (Anderson¹), it was demonstrated that one particular type of SBVG, named 'micro-ramp', has the ability to produce benefits comparable to traditional boundary layer bleed while also offering practical advantages such as physical robustness, low-cost and no power requirements. It should be noted that LES has been recently employed to study oblique shock interactions by Urbin *et al.* 1999², 2000³; Rizzetta *et al.* 2001⁴ and Garnier *et al.*⁵. However, these studies did not investigate flow control techniques such as the micro-ramp device nor did they focus on shock stability and three-dimensional flow control physics. Herein we consider a Mach 3 turbulent boundary layer with $Re_{\delta^*} = 3,800$ with and without an oblique impinging shock with micro-ramps. For these conditions, the turbulent structure response to the micro-ramps and the shock wave was investigated. As a basic study, supersonic boundary layer with shock impingement and the same flow without shock impingement but including a micro-ramp are studied to investigate the characteristics of shock impingement and the micro-ramp interaction with the surrounding flow. Then three different micro-ramp configurations are simulated to study the beneficial effects, such as smaller displacement thickness and improved total pressure recovery.

II. Numerical Methodology

The computational efforts consist of Large Eddy Simulations which provide fine spatial and temporal resolution of the turbulent structures to give a high-fidelity solution with little empiricism. To conduct the present LES studies, unsteady finite volume flow solver called WIND code (developed at AEDC, NASA Glenn) is employed based on the work of Lee *et al.*⁶. The LES studies will be conducted with and without flow control at flow conditions similar to those of experiments at the Air Force Research Laboratory (AFRL) and at the University of Cambridge to validate, compare and for further understanding. However, the LES conditions are limited to low to moderate Reynolds numbers due to computational expense.

2.1 Numerical Schemes and Turbulence Models

To conduct the present LES studies, a third-order upwind scheme combined with min-mod TVD for the convective terms is used. This allows one to obtain high-fidelity eddy and shock capturing flow solutions when combined with a high-resolution structured grid. The temporal integration uses a second order implicit scheme with Newton sub-iteration. For the turbulence, the monotone integrated LES (MILES) approach was employed, where the inherent dissipation in the numerical algorithm is taken as the sub-grid stress model. MILES data for supersonic turbulent boundary layer simulation gave results in close agreement with that of using Smagorinsky sub-grid stress model.² The

time step used for the LES study is $dt = cfl \Delta x / U^\tau$, where Δx is the smallest streamwise cell length and the Courant number, cfl , equals to 0.35 which is sufficiently below the stability threshold of the flow solution. In addition, the Baldwin-Lomax turbulence model was used for RANS simulations with a cfl based on the streamwise cell length of 0.8.

2.2 Rescaling-Recycling Method

Originally developed by Lund *et al.*⁷ for incompressible flows, rescaling-recycling method has been extended for compressible boundary layer flows by Urbin and Knight^{2,3}. This is a key method of generating turbulent inflow condition while removing a significant amount of computational load by eliminating the need to simulate boundary layer flows from the leading edge of the flat plate. Instantaneous flow field at a given downstream location can be rescaled using boundary layer theory such that the rescaled average flow field would match the average flow field at the targeted upstream location. Thus, the rescaled flow field from the given downstream location, or recycle station, can be used as an input at the upstream location, or inlet station, on the condition that the distance between the two stations is sufficiently long; i.e. 1000 wall units⁸. Multilayer scaling⁹ can be used for the boundary layer profile. However, decomposing it into inner and outer layer, similar to Urbin *et al.*^{2,3} is employed in our study. For the average streamwise velocity U , the inner layer profile obeys the law of the wall.

$$U^{inner} = u_\tau(x) \left(\frac{1}{\kappa} \ln(y^+) + C \right) \quad (1)$$

where $y^+ = y u_\tau / \nu_w$ is the wall unit and u_τ is the frictional velocity, ν_w is the kinematic viscosity at the wall. κ is the von Karman constant and C is the empirical constant. Since u_τ is only a function of streamwise coordinate, x , the average stream-wise velocity at the inlet station can be obtained by multiplying the frictional velocity ratio, β .

$$U_{inlet}^{inner} = \beta U_{recycle}^{inner}(y_{inlet}^+) \quad (2)$$

where $\beta = u_{\tau@inlet} / u_{\tau@recycle}$. Note that $U_{recycle}^{inner}$ has been interpolated to the y^+ coordinate system at the inlet station. The outer layer follows the velocity defect law such that the following similarity rule can be applied.

$$U^\infty - U^{outer} = u_\tau(x) f(\eta) \quad (3)$$

where $\eta = y / \delta$ and δ is the boundary layer thickness. Similarly, outer layer of U at the inlet station can be obtained by

$$U_{inlet}^{outer} = \beta U_{recycle}^{outer}(\eta_{inlet}) + (1 - \beta) U^\infty \quad (4)$$

where $U_{recycle}^{outer}$ is interpolated on to the η coordinate system at the inlet station. As for the fluctuation velocity $u' = u - U$, where u is the instantaneous stream-wise velocity, the

rescaled fluctuation velocities for the inner and the outer layer are obtained by the following equations.

$$u_{inlet}^{inner} = \beta u_{recycle}^{inner}(y_{inlet}^+, z, t) \quad (5)$$

$$u_{inlet}^{outer} = \beta u_{recycle}^{outer}(\eta_{inlet}, z, t) \quad (6)$$

The composite equation is then obtained by combining the inner and the outer region of the boundary layer profile using the weighting function.

$$u_{inlet} = (U_{inlet}^{inner} + u_{inlet}^{inner})[1 - W(\eta_{inlet})] + (U_{inlet}^{outer} + u_{inlet}^{outer})W(\eta_{inlet}) \quad (7)$$

where the weighting function⁷ is defined as

$$W(\eta) = \frac{1}{2} \left[1 + \tanh \left(\frac{4(\eta - 0.2)}{0.6\eta + 0.2} \right) / \tanh(4) \right] \quad (8)$$

Rescaling the wall normal (transverse) velocity, v , and the temperature, T , involves similar procedures except for having $\beta = 1$, where as β is set to the same value as the u case for spanwise velocity, w . The pressure at the inlet is assumed constant due to negligible fluctuations⁸, thus the density field at the inlet station can be computed directly from the rescaled temperature.

In this study the initial solution in the recycling domain is based on a RANS mean velocity profile that corresponds to the desired outlet boundary layer thickness. It was found that using inviscid side-wall (instead of spanwise periodic) boundary conditions allowed the instabilities to develop faster. Therefore, the recycling was initially carried out with these sidewalls and then after several sweeps was changed to spanwise periodic conditons until the out flow became statistically stationary with the proper boundary layer thickness. To rescale the flow field at the recycle station to the inlet station coordinate, y_{inlet}^+ and η_{inlet} , the boundary layer thickness ratio and the frictional velocity ratio must be computed priori. These can be estimated from empirical relations given by Smits *et al.*¹⁰. The involved a inner region rescaling given by

$$\frac{u_{\tau, inlet}}{u_{\tau, recycle}} = \left(\frac{\delta_{recycle}}{\delta_{inlet}} \right)^{\frac{1}{10}}$$

However, their outer region re-scaling was method was not found to be generally robust for changes in Mach number and Reynolds number, so that a different technique was employed. Specifically, a feed-back loop was instituted to prescribe the scaling used for recycling to ensure that the final LES boundary layer ratio converged to the RANS boundary layer ratio:

$$\frac{\delta_{recycle}}{\delta_{inlet}} = (\delta_{o,recycle} + \frac{1}{2}(\delta_{current,inlet} - \delta_{o,inlet})) / \delta_{o,inlet}$$

$\delta_{o, inlet}$ and $\delta_{o, recycle}$ are the initial values for the displacement thickness at each stations. Average u profile at the inlet station is updated at each iterations such that $\delta_{current, inlet}$ can be directly computed. The flow field stabilized to the targeted $\delta_{o, inlet}$ at the inlet station as the average u profile converges, whereby the δ ratio becomes a constant.

2.3 Computational Domain

The baseline micro-ramp dimensions are shown in Fig. 1, which was provided by Anderson¹ who investigated different shapes using RANS simulation and concluded the geometry was deemed optimal. As shown in Fig. 2b, the computational domain consists of 11 zones in order to include the complex geometry of the micro-ramp and a oblique shock wedge of angle, γ , that creates a flow deflection, where the each interfacing zones are abutting grids. The dimensions of the domain are based on the ratio of height of the micro-ramp, h , and the reference displacement thickness, δ_{ref}^* . This reference baseline displacement thickness was defined as that for at the theoretical inviscid shock location ($x = x_{IS}$) for a clean flat plate, i.e. with no shock ($\gamma = 0$) and no micro-ramp (NR). This value was obtained from flow solutions using RANS data, for the experimental conditions due to lack of measurement at that location.

An example of the computational domain is shown in Fig. 2, which is a scaled version of the test section of the wind tunnel at AFRL. The length of the domain is $312 \delta_{ref}^*$ and the width of the domain is $23.7 \delta_{ref}^*$ where the height varies from $86.3 \delta_{ref}^*$ to $61.1 \delta_{ref}^*$ at the entrance and the exit of the domain. The micro-ramp trailing edge, whose height is $3.19 \delta_{ref}^*$, is located at $x^* = 57$ upstream of the shock impingement location, where $x^* = (x - x_{IS}) / \delta_{ref}^*$. The first zone (recycling zone), whose length is $29.5 \delta_{ref}^*$, generates turbulent boundary layer inflow conditions using the rescale-recycling method. The super sonic flow enters into the test section where the wedge ($\gamma = 8^\circ$) is placed at the top ceiling generating a 25.6 degree shock wave. This shock wave impinges on the boundary layer at $x^* = 0.0$ and the flow data is measured at $x^* = 86.2$, which corresponds to the location of the pitot tubes in the experiments, as shown in Fig. 2a. The no-slip condition is imposed on the bottom plate and the micro-ramp, whereas the top ceiling has inviscid wall conditions. Periodic boundary conditions are imposed on the side walls to represent arrays of micro-ramps in the spanwise direction, similar to the experiments. The first grid point normal to the bottom wall is at $y^+ = 1$ (based on the shear stress at the inlet station of rescale-recycle zone), where the streamwise grid spacing corresponds to x^+ of 28 and z^+ of 13, resulting in 3.2 million nodes (Fig. 3a). The grid resolution is denser at both the micro-ramp and its posterior to capture the fine vortical structures, as shown in Fig. 3b.

2.4 Spatial Independence and Time Integration Study

A grid resolution study was performed by increasing grid points of the baseline grid by 30 percent for each of the computational coordinate directions (ϵ , η and ζ), resulting in an increase of 2.2 times the total number of nodes. This was defined as the “dense grid”. The results were time-averaged over a finite period once the initial transients had convected downstream. The average for a given variable, ϕ , is defined as

$$\overline{\phi} = \frac{1}{\tau_{int}} \int_t^{t+\tau_{int}} \phi dt \quad (12)$$

where τ_{int} is the total integral time. This quantity can be normalized as $\tau^* = \tau_{int} / \tau_{dom}$, where $\tau_{dom} = L / U_\infty$. L is the streamwise length of the domain and U_∞ is the free-stream velocity. Therefore, τ_{dom} represents the time scale of the flow to convect through the domain, i.e. a single time-sweep, which can be used to non-dimensionalize the integration time. The convergence study of time integration used for averaging was conducted by comparing results from integration time $\tau^* = 4$ and 8. As shown in Fig. 4a and 4c. The average velocity profiles and the average total pressure profile were compared between the solutions from these two grids and small but significant differences were found as shown in Fig. 4b and 4d. The differences in the velocity profiles are amplified in the pressure profile since stagnation pressure profiles are proportional to Mach number to the 7th power for small changes. While there are some grid-resolution effects, the substantial increase in computational time was not deemed necessary to obtain predictions between different micro-ramp configurations. Thus the remaining computations were performed with the base line grid with the integration time of $\tau^* = 4$.

III. Results

Herein we consider a Mach 3 turbulent boundary layer with $Re_{ref} = 3,800$ (based on δ_{ref}^* defined in section II.3), where the free-stream pressure and the temperature were 7076 N/m² and 582.3 K, respectively. The scaled version of AFRL test section, shown in Fig. 2 is used for the computational domain. For these conditions, the turbulent structure solution was obtained for a clean plate (no ramps no shock), as well as for the addition of the shock and the addition of the baseline micro-ramp configuration. Then two other micro-ramp configurations were simulated to study its effects on displacement thickness.

3.1 Supersonic boundary layer flow with micro-ramp and no shock wave

Experimental studies on supersonic turbulent boundary layer flow with micro-ramps and no shock wave were conducted by Cambridge university¹¹. The Mach number is $M = 2.5$ with $Re_{ref} = 33,000$. An initial LES study on the supersonic flow over the micro-ramp with no impinging shocks was compared with the oil streak visualization from the Cambridge experiments to investigate the flow interactions due to the micro-ramp

presence. For the LES and RANS simulations, the Mach number is $M = 3$, with $Re_{ref} = 2,900$. Despite the differences in the Mach number and the Reynolds number, the steady RANS flow and the unsteady flow field from LES provided consistent features of the ramp interaction with the supersonic flow including the shock compression, at the ramp front, expansion waves, at the ramp rear, and wake flow downstream of the ramp. The density contour of the instantaneous flow and the RANS flow solution, shown in Fig. 5b and c, traces of strong shocks formed from the micro-ramp can be observed, similar to the Schlieren image shown in Fig. 5a.

3.2 SBLI with no micro-ramp

The supersonic boundary layer flow with $M=3$ and the oblique shock but without the micro-ramp (NR) was first studied to understand the flow characteristics, such as shock impingement and boundary layer separation characteristics. Fig. 6 shows a streamwise view of the Mach number contour from $x^* = -38.2$ to the end of the computational domain, where traces of the primary shock and its reflection can be seen. The instantaneous LES Mach contour show a complex flow separation at the shock impingement location (especially seen in the $y^+ = 1$ contours) with large-scale spanwise-structures downstream of the interaction. The averaged LES data, however, shows a two-dimensional separation and a uniform boundary layer thickness which is recovering in the streamwise direction. This is qualitatively similar to the RANS result, though the interaction has less distinct features. To investigate streamwise eddies at different locations $x^* = -57, -3.7$ and 86.2 , the instantaneous Mach contours of LES flow solution is shown in Fig. 7 in a spanwise plane. It can be seen that the boundary layer grows in the time-averaged results and in the instantaneous LES results, where larger structures with wider spacing are observed. Predictions and measurements of the velocity profiles at the WPAFB measuring plane are shown in Fig. 8. The results indicate show that the LES results have closer agreement with the low Reynolds number ($Re_{ref} = 3,990$) experimental data than the RANS results, which is closer to the high Reynolds number ($Re_{ref} = 13,000$) experimental data. This is due to the calibration in the Baldwin-Lomax turbulence model to predict flows at higher Reynolds number. Thus, it makes sense that the LES and low Reynolds number experimental data agree well, since their Reynolds numbers are similar.

3.3 SBLI with micro-ramp

The next studies investigated the addition of the baseline ramp (BR) to the above SBLI. In Fig. 9, the streamwise view of the Mach number contours located at the middle of two periodic micro-ramps is shown, where the LES results show a fair amount of flow separation, whereas the RANS result contains smaller region of separation. The LES results also show that the size of the spanwise vortical structures downstream of the shock impingement location have decreased in comparison to the results for no ramp shown in Fig. 6 LES. The streamwise velocity contour, u , extracted from $y^+ = 1$ shows the positive stream of flow cuts through the separated region, which indicates the benefits of using the micro-ramp. In comparison with LES and averaged LES, RANS result shows

different shapes of the separated region and a smaller area of positive flow that divides the separation. Mach contour at the trailing edge of the micro-ramp, $x^* = -57$, shown in Fig. 10, reveals that two strong streamwise vortical structures are generated via the corner flow effect from the side walls of the micro-ramp and the floor¹². The two vortical tubes merge together to create a larger tube with two counter rotating vortices inside, as shown in Fig. 10 at $x^* = -3.7$, which is taken from one cord downstream of the micro-ramp. This vortical tube locally thins the boundary layer on both sides of the tube, which convects through the shock impingement and wipes out the separated flow in its path. This can help reduce the amount of bleed necessary to maintain the flow stability. The cross-sectional view of Mach contours at the measuring station reveals that boundary layer from RANS is thicker than the LES result.

The velocity profiles are shown in Fig. 11 for each rake location. Rake 1 is located at $z^*=11.85$ from the center of the domain (middle of two micro-ramps) and rake 2 is at $z^*=9.7$, which is at the tip of the leading edge. Rake 3 position is at $z^*=7.5$ ($z^* = (z - z_{rc})/\delta_{ref}^*$, where z_{rc} is at the micro-ramp center). The u profiles from LES results show close agreement with the low Reynolds number experimental data, particularly at rake 2. In particular, the experiments showed variations between different rake positions than shown by the LES results and a somewhat fuller profile both close to the wall and at y^* of about 4 ($y^*=(y - y_{wall})/\delta_{ref}^*$, where y_{wall} is at the floor of the domain). These differences are qualitatively similar to those shown for the high-resolution grid case (Fig. 4) indicating improved resolution may be desirable, but in general the experimental trends were reasonably predicted. The RANS results substantially under-predicted the velocity profiles, consistent with the no control case (Fig.8). Thus, LES will only be used for the remaining simulations.

3.4 Micro-ramp size and location

To study the effects of different micro-ramp size and the location, two other cases were investigated to compare with the above baseline ramp (BR) configuration and the no ramp (NR) case. One is a 50% smaller micro-ramp at the same location (HR) as the previous study and the other is to use 50% smaller micro-ramp whose trailing edge is now moved up to the half-point between the original micro-ramp's trailing edge and the shock impingement location (HRHD). The purpose of HRHD case is to investigate the benefits of sustaining strong streamwise vortices through the shock impingement region, which may contribute to eliminating flow separation. The flow separation areas have decreased for the two smaller micro-ramp cases (HR and HRHD in Fig. 12) in comparison to the original micro-ramp case (BR in Fig. 9). The height of the separation zone is minimal for HR, whereas the overall separation area is minimal for HRHD, as shown in Fig. 12. The averaged LES Mach contour (Fig. 13) reveals that the boundary layer thickness has slightly decreased for HR and HRHD in comparison with BR. This may be attributed to the BR (with a height of $3.19 \delta_{ref}^*$) more substantially interacting with the supersonic portion of the flow since that the supersonic region of the boundary layer occurs for y^* below 0.5. This can lead to increased stagnation pressure losses and

increased vortex shedding. The larger flow disturbances caused by the original micro-ramp (BR) can be visually seen in the instantaneous Mach number contour in Fig. 13.

IV. Conclusions

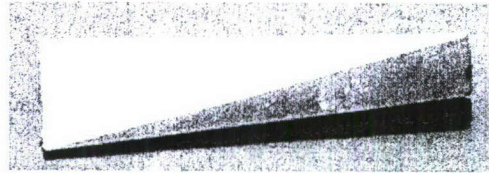
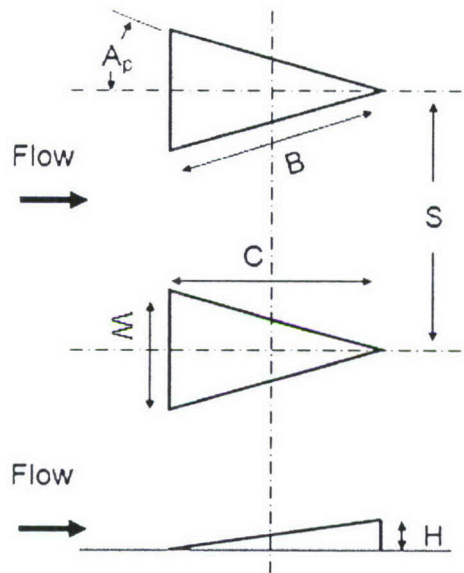
A study on supersonic boundary layer flow control using micro-ramp has been presented. A simplified rescale-recycle algorithm for compressible flows is used to generate turbulent inflow conditions which reduce computational cost by eliminating the need to compute boundary layer flows from the leading edge of the flat plate. In general, the LES and RANS results captured the qualitative fluid physics of the interaction, but only the LES gave quantitative predictions of the velocity profiles downstream of the interaction. However, the LES simulations required approximately three-fold increase in computing time.

Supersonic boundary layer with micro-ramp showed that the streamwise vortical structures tends to reduce and/or break-up the separated flow region caused by the shock impingement. Different sizes and locations for the micro-ramp were studied, which showed that smaller micro-ramp (HR) and the same one located closer to the shock impingement (HRHD) produced less disturbances in the flow which creates a thinner displacement thickness and higher stagnation pressure recovery in comparison to baseline ramp case. HRHD significantly reduced the area of separation, which is a promising result. However, further study on micro-ramp performance (under different Reynolds numbers, shock strengths, and boundary layer inflows) is needed before specific recommendations can be made.

V. References

- ¹Anderson, B., Tinapple, J. and Surber, L., "Optimal Control of Shock Wave Turbulent Boundary Layer Interactions Using Micro-Array Actuation," *AIAA Fluids Engineering Conference*, June 2006, San Francisco.
- ²Urbin, G., Knight, D., and Zheltovodov, A.A., "Compressible Large-Eddy Simulation using Unstructured Grid: Supersonic Turbulent Boundary Layer and Compression Corner," *AIAA 99-0427*.
- ³Urbin, G., Knight, D., and Zheltovodov, A.A., "Large-Eddy Simulation of a Supersonic Compression Corner, Part I," *AIAA 2000-0398*.
- ⁴Rizzetta, D.A., Visbal, M.R. and Gaitonde, D.V., "Large-Eddy Simulation of Supersonic Compression-Ramp Flow by High-Order Method," *AIAA Journal*, Vol. 39, No. 12, pp. 2283-2292.
- ⁵Garnier, E. and Sagaut, P., "Large Eddy Simulation of Shock/Boundary-Layer Interaction," *AIAA Journal*, Vol. 40, No. 10, pp. 1935-1944.
- ⁶Lee, S., Loth, E., Wang, C. and Kim, S., "LES of Supersonic Boundary Layers μ VG's", *AIAA-2007-3916*
- ⁷Lund, T., Wu, X., and Squires, K., "Generation of Turbulent Inflow Data for Spatially-Developing Boundary Layer Simulations," *Journal of Computational Physics*, Vol. 140, No. 2, 1998, pp. 233-258
- ⁸Cantwell, B., "Organized Motion in Turbulent Flow," *Annual Review of Fluid Dynamics*, Vol. 13, 1981, pp.457-515
- ⁹Fernholz, H., and Finley, P., "A Critical Commentary on Mean Flow Data for Two-Dimensional Compressible Turbulent Boundary Layers," *Tech. Rept. 253, AGARD*, May 1980.
- ¹⁰Smits, A., and Dussauge, J.P., "Turbulent Shear Layers in Supersonic Flow," *American Inst. Of Physics*, New York, 1996, Chap. 2.
- ¹¹Pitt Ford, C.,W., Babinsky, H., "Micro-Ramp Control for Oblique Shock Wave / Boundary Layer Interactions", *AIAA-2007-4115*
- ¹²Rizzetta, D.A., Visbal, M.R. and Gaitonde, D.V., "Large-Eddy Simulation of Supersonic Compression-Ramp Flow by High-Order Method," *AIAA Journal*, Vol. 39, No. 12, pp. 2283-2292.

VI. Figures



$$H = 3.19 \delta^*$$

$$S = 7.5H = 23.93\delta^*$$

$$B = 7.2H = 22.97\delta^*$$

$$C = 6.57H = 20.95\delta^*$$

$$W = 2.92H = 9.31\delta^*$$

$$A_p = 24^\circ$$

Fig. 1 Dimensions of micro-ramp

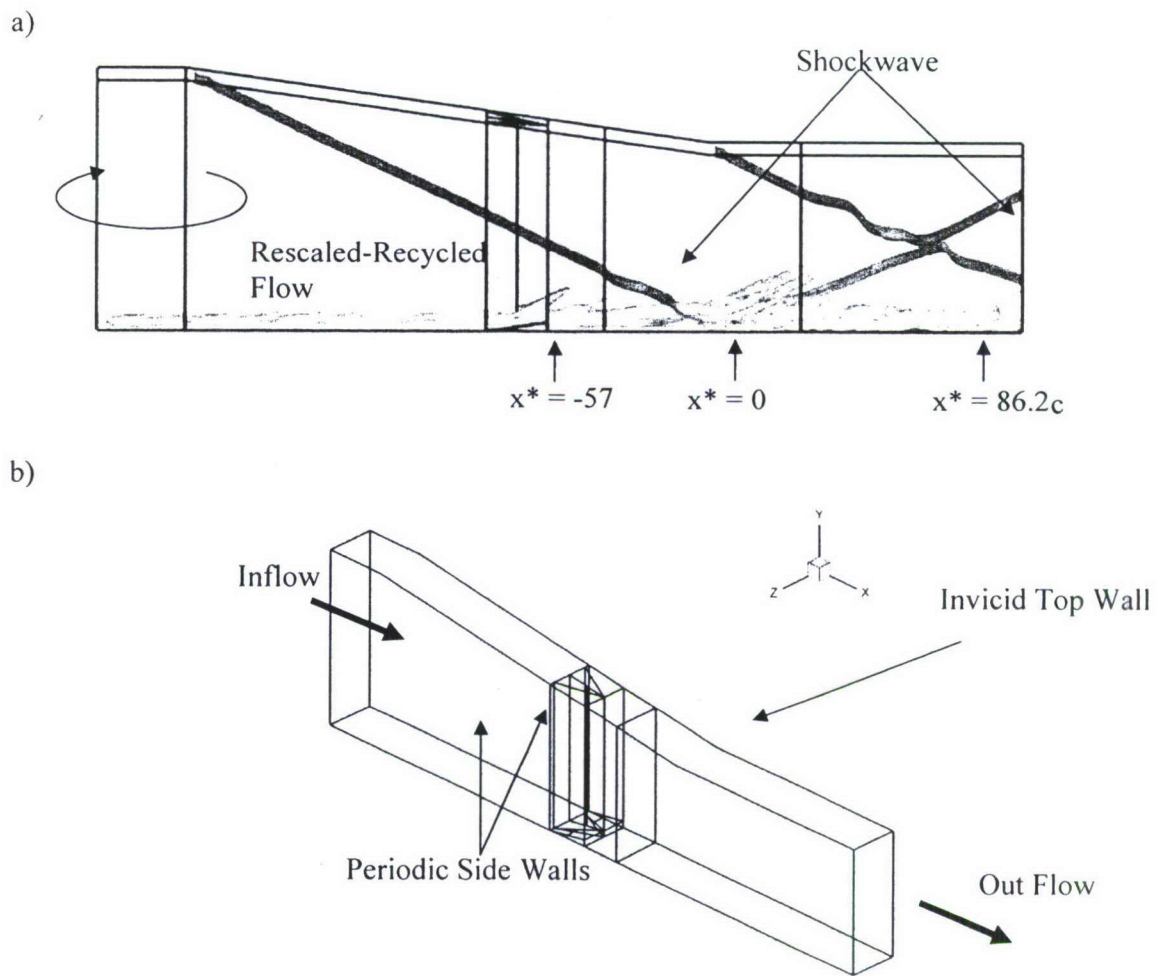


Fig. 2 Boundary conditions a) with shock and expansion waves location and rescaled-recycled zone, and b) isometric view of the domain's skeleton

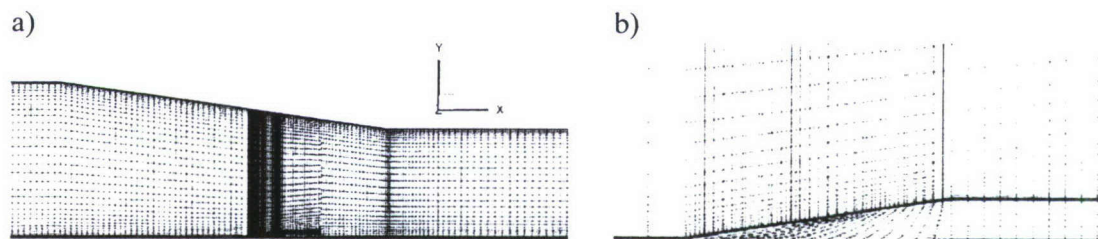
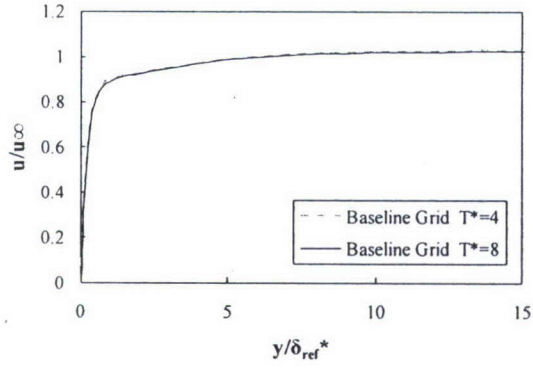
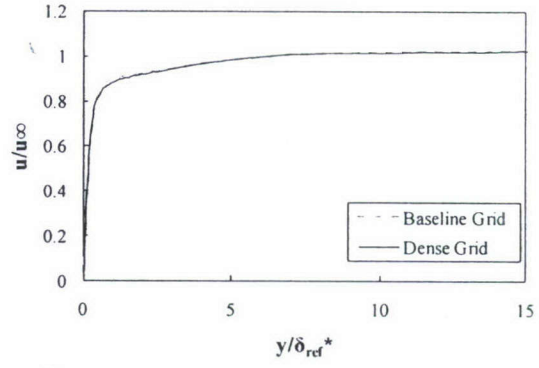


Fig. 3 Grid composition of the domain for a) side view of overall grid, and b) zoom in of grid at the ramp

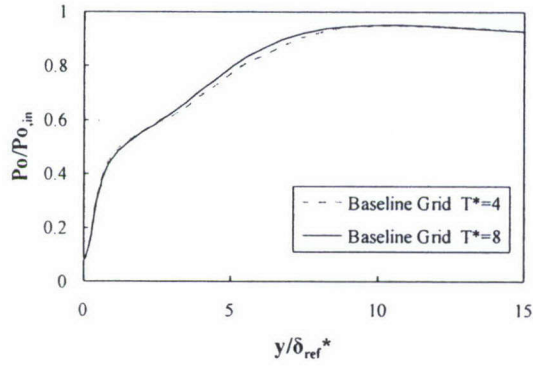
a)



b)



c)



d)

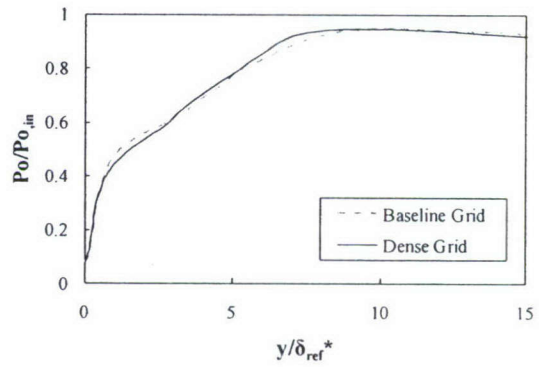
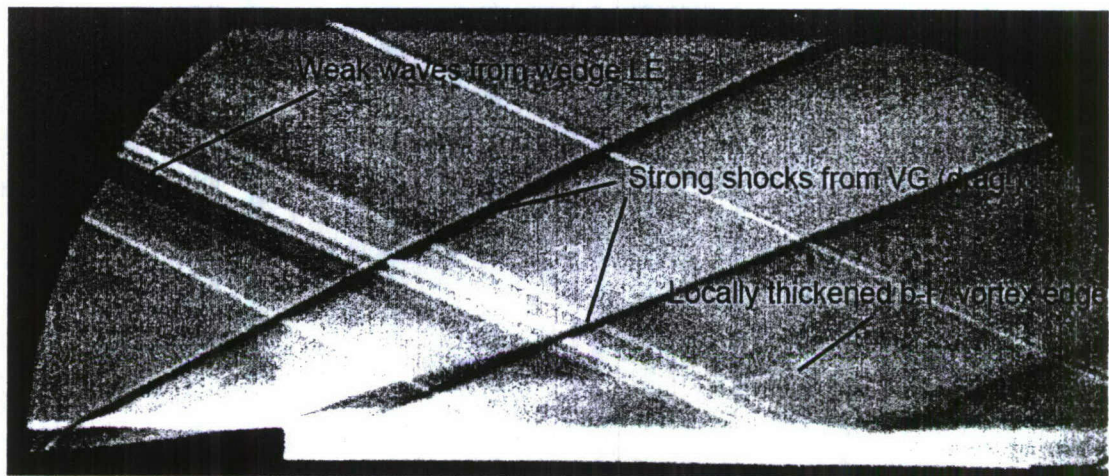
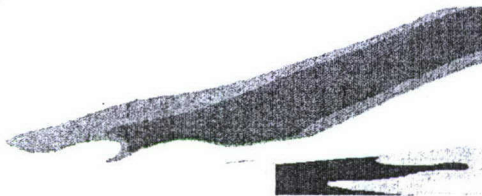


Fig. 4 a) time resolution on velocity profile, b) grid resolution on velocity profile, c) time resolution on total pressure profile, and d) grid resolution on total pressure profile

a)



b)



c)

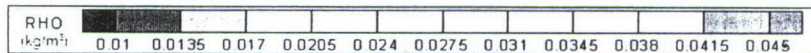
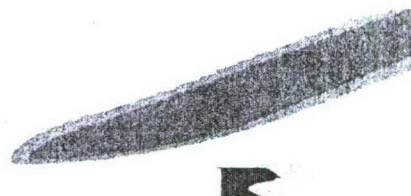


Fig. 5 a) Schlieren image of shock and expansion waves due to the micro-ramp by Pitt Ford *et al*¹¹, and b) instantaneous image of density contour using LES model, and c) density contour using RANS model.

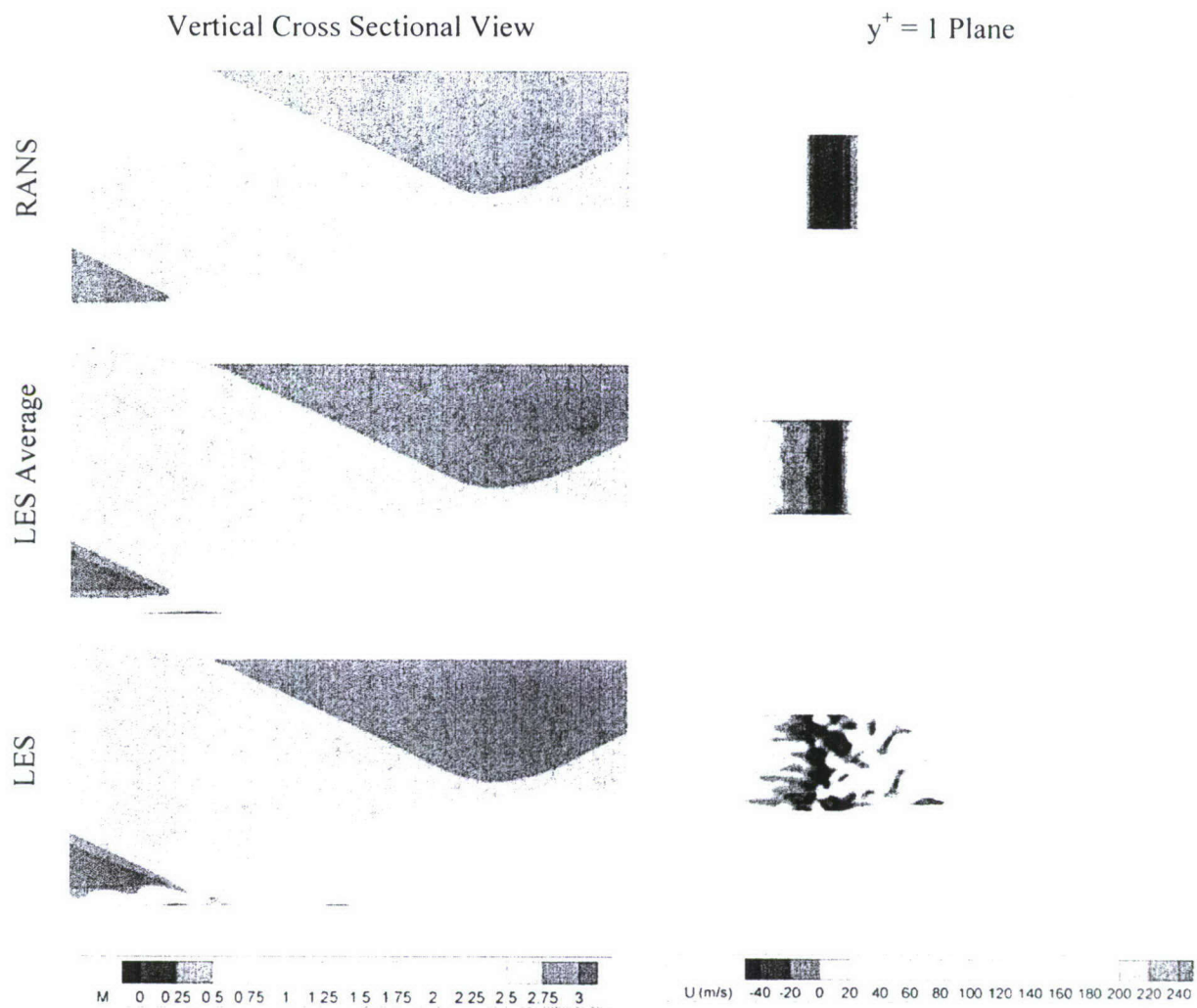


Fig. 6 Mach and streamwise velocity contours of cross sectional and near-surface plane without micro-ramps (NR).

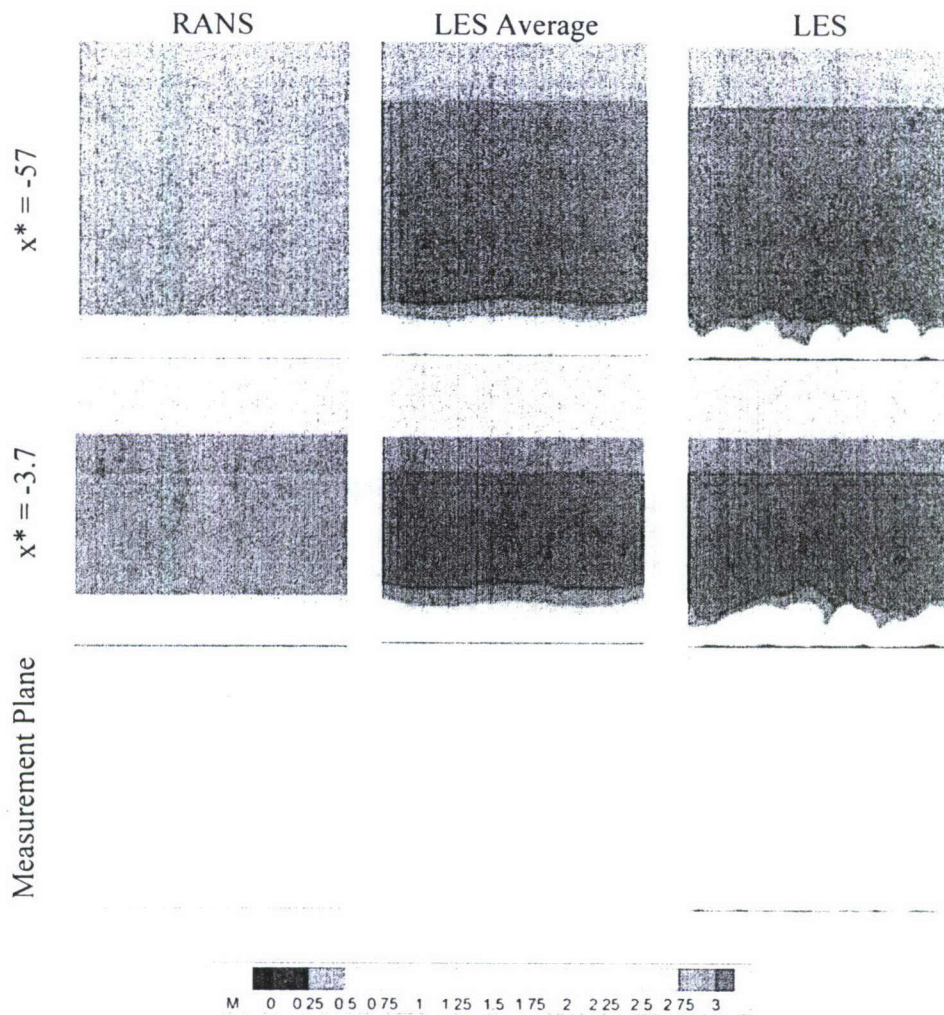


Fig. 7 Mach contours of spanwise plane at various location (NR).

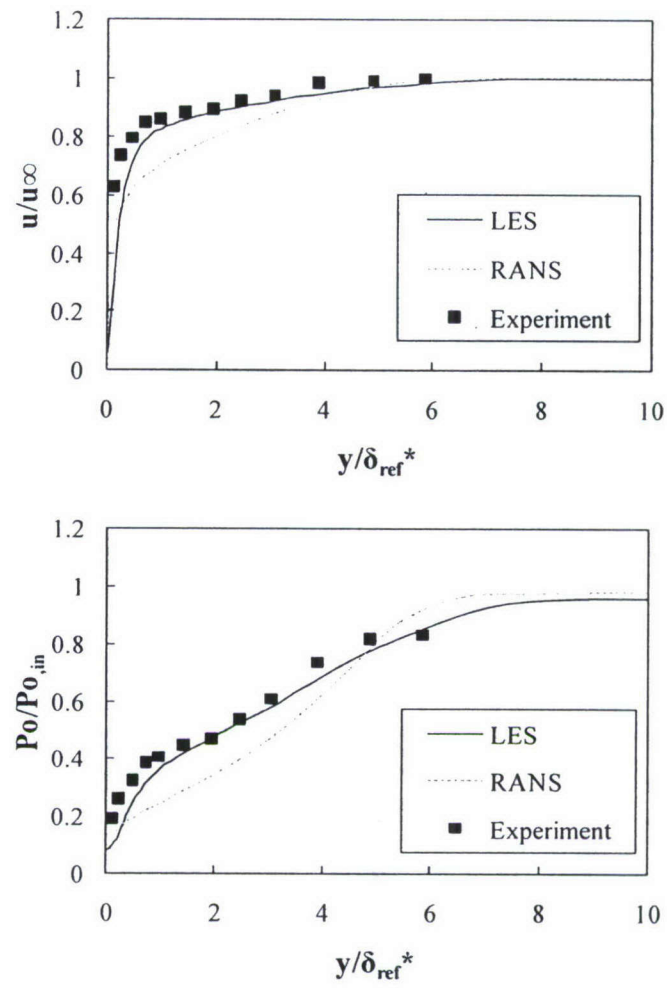


Fig. 8 Comparison between RANS, LES model and the experimental data (Wright Patterson AFB, private communication) for NR model.

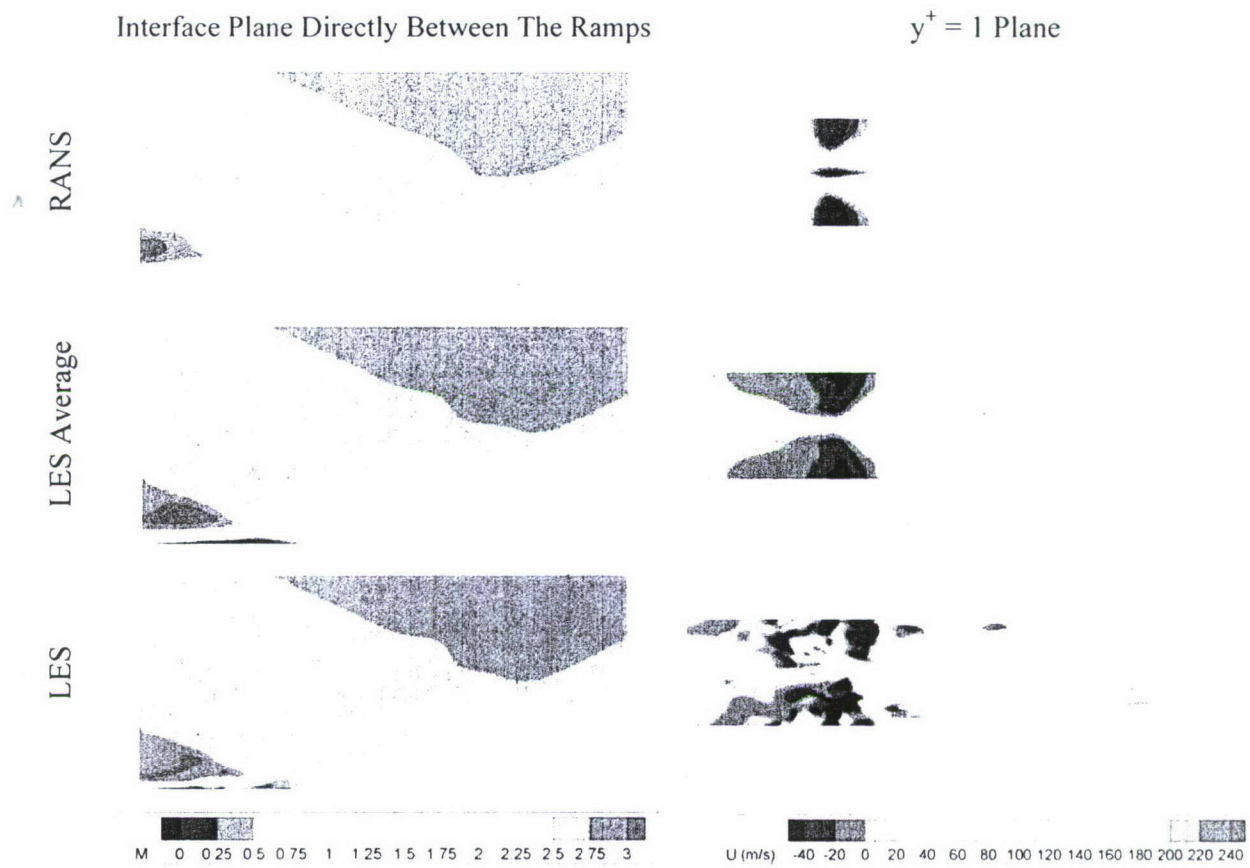


Fig. 9 Mach and streamwise velocity contour of cross sectional plane with the base line micro-ramp (BR).

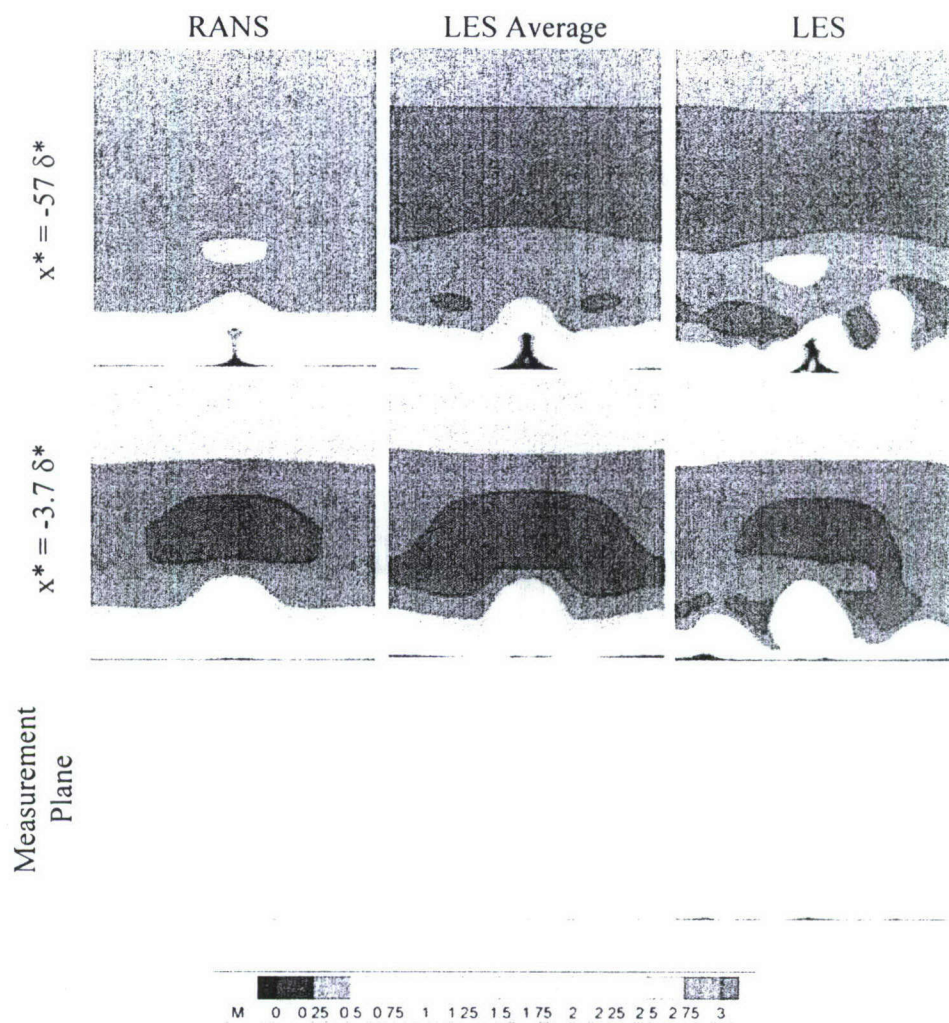


Fig. 10 Mach contour of spanwise plan for various streamwise locations (BR).

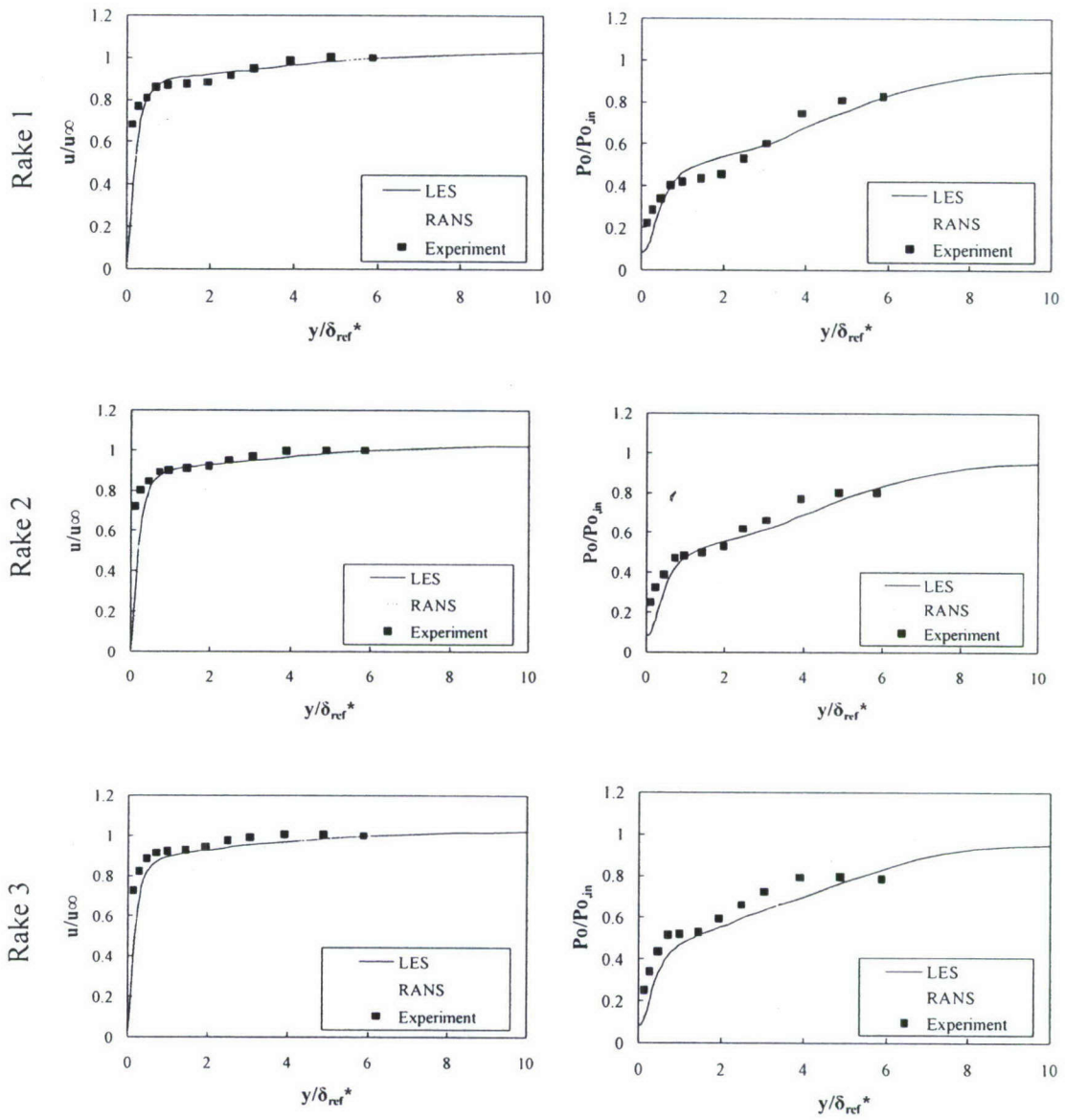


Fig. 11 Comparison of supersonic boundary layer between LES solutions, RANS, and Experimental data (Wright Patterson AFB, private communication) for BR model.

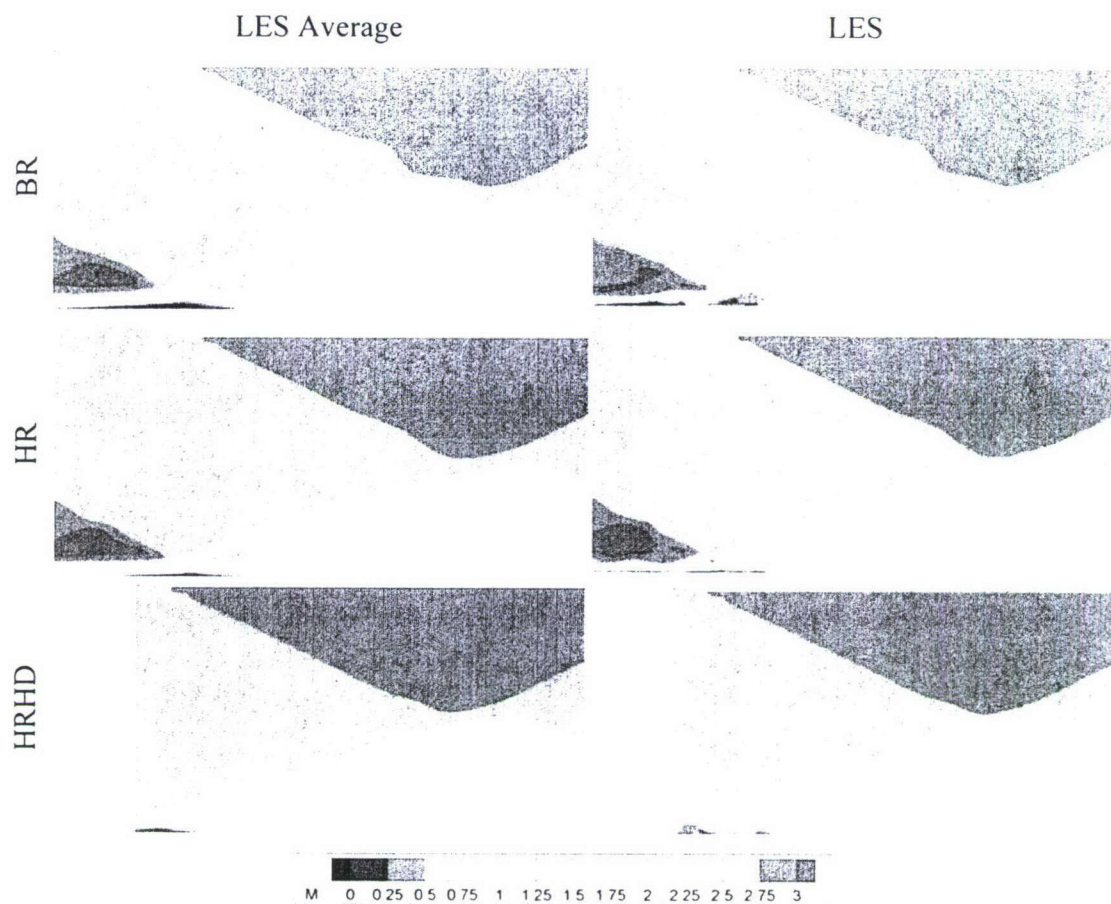


Fig. 12 Visualization of interface plane right between ramps.

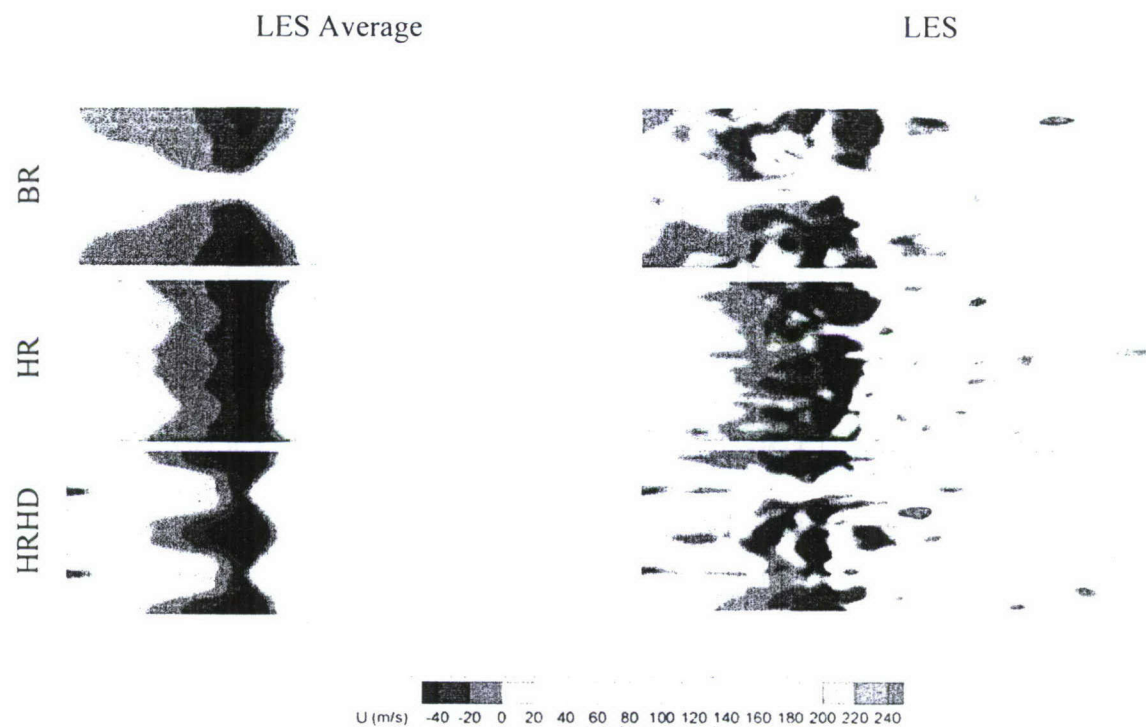


Fig. 13 Steamwise velocity contours at $y^+=1$ plane for three ramp configuration (BR, HR and HRHD) using LES.

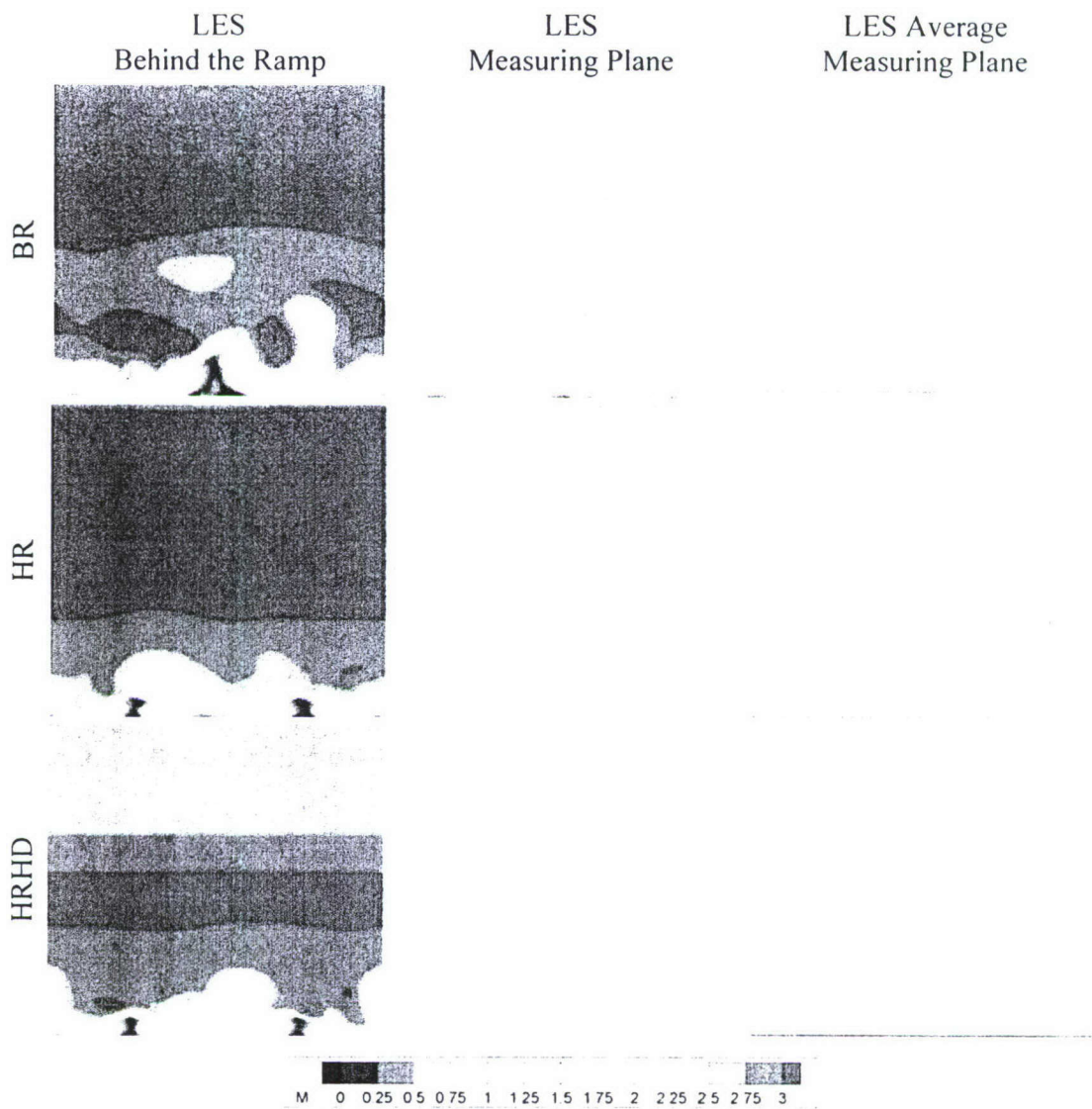


Fig. 14 Mach contour of spanwise plane for BR, HR and HRHD

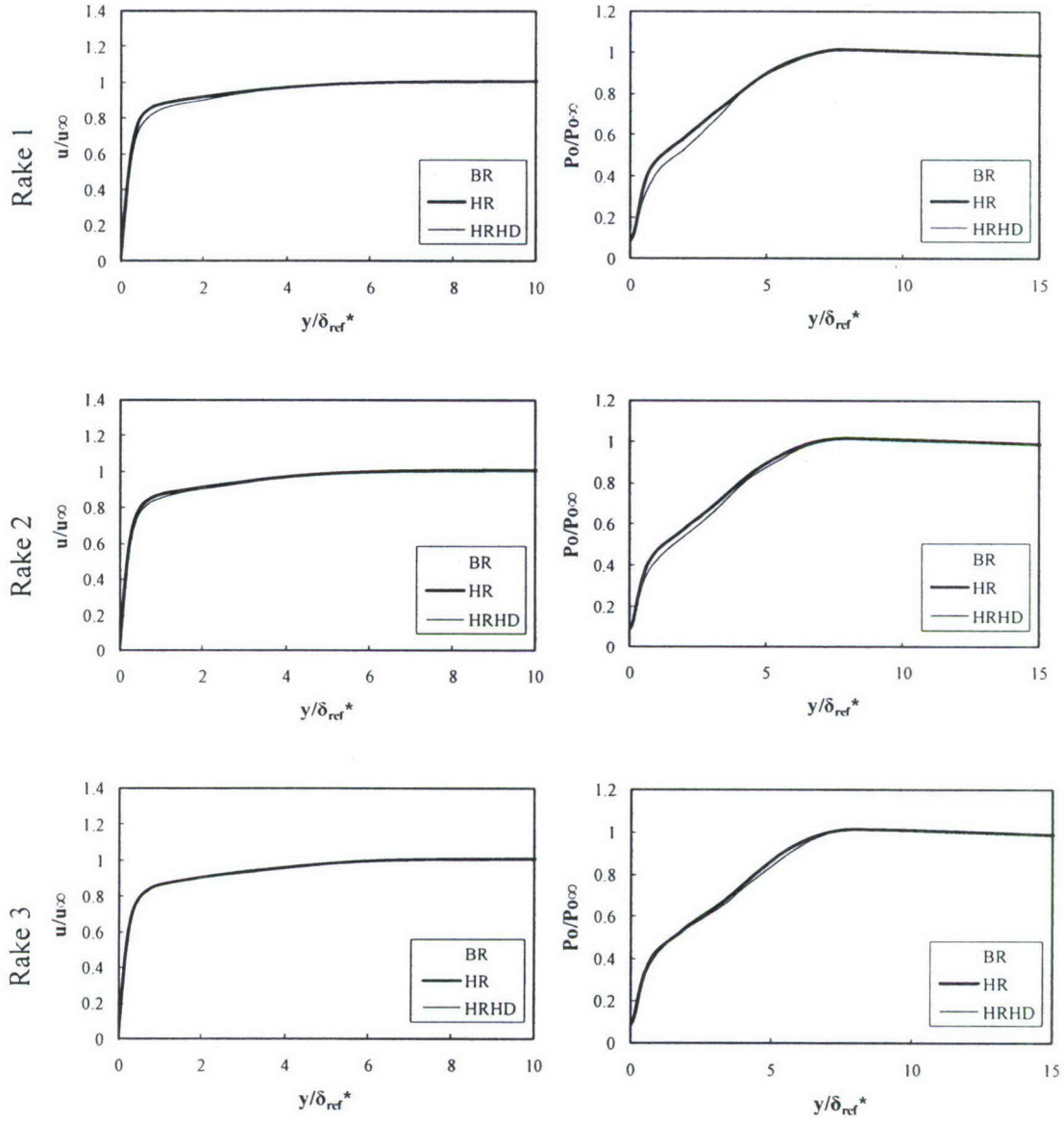


Fig. 15 Comparison of flow solutions between Baseline-Ramp, Half-Ramp, and Half-Ramp-Half-Distance cases.

Table 1.

	BR	BR	HR	HRHD
Mach #	2.5	3.0	3.0	3.0
α/α_{NR}	0.97	0.96	1.07	1.06
δ^*/δ_{NR}^*	0.91	1.05	1.04	1.02
H	1.30	1.23	1.24	1.24
$L_{sep}/L_{sep_{VR}}$	1.12	1.18	0.99	0.69